Research Article Vol. 32, No. 6 / 11 Mar 2024 / Optics Express 10204

Optics EXPRESS

Shipborne single-photon fluorescence oceanic lidar: instrumentation and inversion

MINGJIA SHANGGUAN,* YIRUI GUO, AND ZHUOYANG LIAO

State Key Laboratory of Marine Environmental Science, College of Ocean and Earth Sciences, Xiamen University, Xiamen 361102, China
*mingjia@xmu.edu.cn

Abstract: Laser-induced fluorescence (LIF) technology has been widely applied in remote sensing of aquatic phytoplankton. However, due to the weak fluorescence signal induced by laser excitation and the significant attenuation of laser in water, profiling detection becomes challenging. Moreover, it remains difficult to simultaneously retrieve the attenuation coefficient (K_{lidar}^{mf}) and the fluorescence volume scattering function at 180° (β_f) through a single fluorescence lidar. To address these issues, a novel all-fiber fluorescence oceanic lidar is proposed, characterized by: 1) obtaining subsurface fluorescence profiles using single-photon detection technology, and 2) introducing the Klett inversion method for fluorescence lidar to simultaneously retrieve K_{lidar}^{mf} and β_f. According to theoretical analysis, the maximum relative error of β_f for the chlorophyll concentration ranging from 0.01 mg/m^3 to 10 mg/m^3 within a water depth of 10 m is less than 20%, while the maximum relative error of K_{lidar}^{mf} is less than 10%. Finally, the shipborne single-photon fluorescence lidar was deployed on the experimental vessel for continuous experiments of over 9 hours at fixed stations in the offshore area, validating its profiling detection capability. These results demonstrate the potential of lidar in profiling detection of aquatic phytoplankton, providing support for studying the dynamic changes and environmental responses of subsurface phytoplankton.

1. Introduction

Marine phytoplankton are the most important primary producers in the ocean, initiating the flow of energy and cycling of matter in ecosystems, making them a primary focus of research in biological oceanography. Since the 1970s, a series of ocean color satellites have been launched, providing valuable phytoplankton products that have played a significant role in biological oceanography and global change studies, leading to an unprecedented understanding of global spatiotemporal variations in phytoplankton dynamics. These advancements have deepened our understanding of biological resource distribution, ecological processes, and phytoplankton diversity in large-scale marine ecosystems [1]. They have also provided valuable insights into global marine primary productivity [2], carbon storage capacity, and the mechanisms behind phytoplankton blooms and harmful algal blooms [3]. However, these measurements are limited to clear sky, day-light, high sun elevation angles, and are exponentially weighted toward the ocean surface. Fortunately, lidar has emerged as a stronger candidate due to its greater penetration depth, which is three times deeper than that of passive ocean color, and its ability to continuously profile water bodies day and night [4], position it as a crucial complement to passive ocean color [5].

In the field of lidar for remotely sensing phytoplankton, there are two main techniques: elastic oceanic lidar and laser-induced fluorescence lidar. Elastic lidar can obtain important parameters such as the backscattering coefficient (b_{bp}) [6,7] and the light attenuation coefficient (K_d) [8] by analyzing the 180° volume scattering function (β), lidar attenuation coefficient (K_{lidar}), and polarization ratio (δ). Parameters related to phytoplankton, such as particulate organic carbon (POC) [9,10], phytoplankton carbon [11], and chlorophyll concentration (Chl) [12], can be

#515477 https://doi.org/10.1364/OE.515477
Journal © 2024 Received 8 Dec 2023; revised 12 Jan 2024; accepted 9 Feb 2024; published 6 Mar 2024

Optics EXPRESS

derived using empirical formulas based on b_{bp}, K_d, and δ. On the other hand, fluorescence lidar can directly monitor phytoplankton itself. However, despite the widespread use of fluorescence lidar systems in applications such as historical monuments [13], insect monitoring [14], and vegetation [15], there are still limitations in remote sensing monitoring of phytoplankton. This is mainly due to two reasons: Firstly, the fluorescence induced by laser in phytoplankton occurs in the red-light spectrum, with a central wavelength of $\sim$ 685 nm, where the light is heavily absorbed in water; secondly, the fluorescence backscattered signal is relatively weak compared to the elastic backscattered signal, so even with a high-power laser, only surface fluorescence information of the water body can be obtained [16–21]. Fortunately, through the enhancement of detection sensitivity to the single-photon level, lidar technology has achieved the capability to profile weak signal energy under the constraints of low laser pulse energy and a small aperture telescope. Consequently, this technological advancement has found successful applications in various domains such as atmospheric studies [22], water Raman profiling [23], and standoff underwater oil detection [24]. Notably, the utilization of single-photon detection technology in fluorescence lidar has demonstrated its effectiveness in profiling and detecting weak fluorescence backscattered signals, as evidenced by Refs. [25,26].

However, a challenge remains in inferring two unknown parameters, the fluorescence lidar attenuation coefficient (K_{lidar}^{mf}), and the fluorescence volume scattering function at 180 ° (β_f), from a single measurement after obtaining the profile data from the fluorescence lidar. To address this problem, recent research has proposed a method of adding a Raman channel of water alongside the fluorescence channel. This approach reduces the differential lidar attenuation coefficient and enables the use of perturbation methods to invert β_f [26,27]. In this study, we verified that the Klett inversion method can be used to simultaneously obtain β_f and K_{lidar}^{mf} by studying the power-law relationship between β_f and K_{lidar}^{mf} in fluorescence lidar. Furthermore, we investigated that the quantum yield of phytoplankton (Φ_c) has no effect on the power-law terms of these two parameters, further validating the feasibility of using the Klett inversion method [28]. Through theoretical analysis, we confirmed the accuracy of this method for inverting these two parameters. Additionally, by utilizing the relationship between beam attenuation coefficient (c_{mf}) and K_{lidar}^{mf} established using a Monte Carlo (MC) simulation, as well as the relationship between β_f and phytoplankton absorption coefficients (a_{ph}), the fluorescence lidar can simultaneously obtain c_{mf} and a_{ph}. Note that the c_{mf}, which signifies the rate at which light is absorbed and scattered in seawater, is crucial for estimating parameters such as POC in the water column. Finally, we conducted a 9-hour field experiment in an offshore area to verify the effectiveness of this method.

The article is organized as follows. We first introduce the all-fiber single-photon fluorescence lidar technology, followed by the methodology, including the study of the power-law relationship between β_f and K_{lidar}^{mf}. Next, we analyze the error distribution through theoretical analysis. Finally, we present the results of a field experiment to validate the robustness and feasibility of the algorithm and lidar system.

2. Single-photon fluorescence lidar

As shown in Fig. 1, the single-photon fluorescence lidar system consists of three subsystems: a 532 nm picosecond pulse laser, a telescope, and a detection and data acquisition system. The transmitter of this lidar system utilizes a fiber-based picosecond pulse laser based on the master oscillator power amplifier (MOPA) architecture, with the seed light being a single longitudinal mode picosecond 1064 nm laser. The seed laser is amplified by a single-mode ytterbium-doped fiber amplifier (SM-YDFA) and a high-power ytterbium-doped fiber amplifier (HP-YDFA), and then the lithium borate crystal (LBO) converts the fundamental frequency 1064 nm laser to a 532 nm laser. Additionally, the residual fundamental 1064 nm light is separated using a dichroic mirror (DM). Finally, the generated 532 nm laser has a pulse width of 501 ps, a repetition frequency of 1 MHz, an output average power of 1.0 W, a divergence angle of 0.5 mrad, and a spectral width of 0.04 nm.

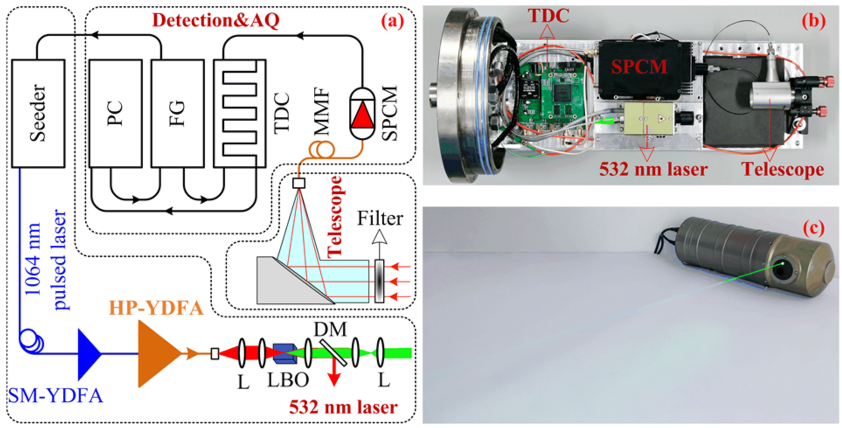

Fig. 1. (a) Optical layout of the single-photon fluorescence lidar. SM-YDFA: single-mode ytterbium-doped fiber amplifier; HP-YDFA: high-power ytterbium-doped fiber amplifier; L: lens; LBO: lithium borate; DM: dichroic mirror; MMF: multimode fiber; SPCM: single photon counting module; Detection & AQ: detection and data acquisition system; TDC: time-to-digital converter; FG: function generator; PC: personal computer. (b) Internal photo of the single-photon fluorescence lidar. (c) Photo of the single-photon fluorescence lidar.

The laser incident on the water interacts with the phytoplankton in the water, inducing fluorescence. Among them, the induced fluorescence backscattering signal is coupled into a 105 µm multimode fiber (MMF) through a numerical aperture (NA) 0.22. This coupling is achieved using an achromatic lens (Thorlabs RC12FC) with a focal length of 50.8 mm and an effective aperture of 22.4 mm, resulting in a narrow field of view of approximately 2.1 mrad. As shown in Fig. 1, the lidar system adopts a design with separate transmitter and receiver, with a distance of approximately 30 mm between the laser transmitter and the receiving lens, and the geometric overlap factor reaches 100% at a distance of about 7 m. In this work, the lidar is deployed on a ship with a distance of approximately 10 m from the water surface, so the geometric overlap factor of the water backscattered signal is 100% in the subsequent data inversion process.

To isolate the strong 532 nm elastic backscattered signal and extract the nearby 685 nm fluorescence signal, three fluorescence filter slices with a central wavelength of 685 nm and a bandwidth (full width at half maximum) of 10 nm are serially connected in front of the optical telescope. These filters provide a total isolation of 150 dB for the 532 nm elastic signal, and the total transmittance of the three filter slices is greater than 50%. It should be noted that due to the wide spectral width of the laser-induced phytoplankton fluorescence, a larger bandwidth can enhance the reception of fluorescence backscattering signals and improve signal-to-noise ratio (SNR). However, due to the use of a highly sensitive single-photon detector and background noise interference (such as signal lights on the research vessel and moonlight), a wider bandwidth results in stronger background noise. A wider bandwidth can also lead to interference from fluorescence signals induced by other substances (such as oil). Therefore, a bandwidth of 10 nm was chosen in this study. When the background noise on the platform is low and the fluorescence signals induced by negligible other substances, it is possible to consider using fluorescence filters with a larger bandwidth.

Finally, the extracted fluorescence backscattering signal is detected using a free-running single photon counting module (SPCM: Excelitas SPCM-AQRH-15), continuously counting individual photons without being constrained by specific time intervals or synchronization to external signals. The detection efficiency of the SPCM is 62% at 685 nm, with a dark count of 50 counts per second (cps). In addition, a self-developed time-to-digital converter (TDC) with a resolution of 500 ps is used to accurately capture the time information of the fluorescence backscattered photons [25]. The electronic module employs a self-built function generator (FG) implemented on a field-programmable gate array (FPGA) to generate precise control signals for the laser and TDC.

3. Methodology

3.1. Formula derivation

The backscatter profile of the fluorescence lidar through a fluorescence filter can be expressed as the convolution (⊗) of the backscatter profile [29] and the filter, as follows:

$$P_f(\lambda_f, \sigma_f, z) = \frac{B_f \cdot Q_f(z)}{(n \cdot H + z)^2} \cdot \beta_f(\lambda_f, z) \otimes g(\lambda_f, \sigma_f) \cdot \exp\left\{-\int_0^z [K^m_{lidar}(y) + K^f_{lidar}(y)]dy\right\}, \quad (1)$$

where P_f represents the water fluorescence backscattered signal at a depth of z, given an emitted laser wavelength (λ_L) of 532 nm and a fluorescence wavelength (λ_f) of 685 nm; H represents the height at which the lidar is positioned above the water surface, which is 10 m in this case; n represents the refractive index indicator of the water; B_f is a constant that includes lidar parameters independent of depth, such as the output laser power, quantum efficiency of the detector, and transmittance of the optical transceiver system; Q_f (z) represents geometric overlap factor; β_f represents the volume scattering function at 180° for chlorophyll fluorescence at a wavelength of 685 nm; $g(\lambda_f,\ \sigma_f)$ represents the transmittance function of a custom-made fluorescence filter, which can be approximated as a Gaussian function with a center wavelength of λ_f and a bandwidth of σ_f; K^m_{lidar} represents the attenuation coefficient of the lidar at 532 nm; K^f_{lidar} represents the attenuation coefficient of the lidar at 685 nm.

Taking the natural logarithm of the backscattered signal squared depth yields:

$$S(\lambda_f, \sigma_f, z) = \ln[P_f(\lambda_f, \sigma_f, z) \cdot (n \cdot H + z)^2], \quad (2)$$

$$S(\lambda_f, \sigma_f, z_0) = \ln[P_f(\lambda_f, \sigma_f, z_0) \cdot (n \cdot H + z_0)^2], \quad (3)$$

where z_0 is the depth of the first point of signal. By making the difference between Eq. (2) and Eq. (3), we can get:

$$\begin{aligned} S(\lambda_f, \sigma_f, z) - S(\lambda_f, \sigma_f, z_0) &= \ln\left[\frac{P_f(\lambda_f, \sigma_f, z) \cdot (n \cdot H + z)^2}{P_f(\lambda_f, \sigma_f, z_0) \cdot (n \cdot H + z_0)^2}\right] \\ &= \ln\left[\frac{\beta_f(\lambda_f, z) \otimes g(\lambda_f, \sigma_f)}{\beta_f(\lambda_f, z_0) \otimes g(\lambda_f, \sigma_f)}\right] - \int_{z_0}^{z} K^{mf}_{lidar}(y)dy \end{aligned}, \quad (4)$$

where K^{mf}_{lidar} $(z) = K^m_{lidar}$ $(z)+$ K^f_{lidar} (z).

Theoretical analysis suggests that when the $d\beta/dz<1.6 \cdot 10^{-9}$, the retrieved error of β_f is within 20%, and the Klett method is not required. Then, K^{mf}_{lidar} (z) can be determined by solving Eq. (4) using the slope method [30]:

$$K^{mf}_{lidar}(z) = -\frac{dS(\lambda_f, \sigma_f, z)}{dz} = -\frac{d\{\ln[P_f(\lambda_f, \sigma_f, z) \cdot (n \cdot H + z)^2]\}}{dz}, \quad (5)$$

However, if the water is inhomogeneous ($d\beta/dz \geq 1.6 \cdot 10^{-9}$), it becomes necessary to assume regarding the relationship between β_f and K^{mf}_{lidar} in order to solve for the unknown quantity in

Optics EXPRESS

Eq. (4). After analysis, which will be further elaborated, β_f and K_{lidar}^{mf} approximately satisfy the following power law relationship:

$$\beta_f(\lambda_f, z) = const \cdot [K_{lidar}^{mf}(z)]^k, \tag{6}$$

where *const* is a constant and k is the power exponent. After that, by differentiating Eq. (4) we can get:

$$\begin{aligned} \frac{dS(\lambda_f, \sigma_f, z)}{dz} &= \frac{1}{\beta_f(\lambda_f, z)} \cdot \frac{d[\beta_f(\lambda_f, z)]}{dz} - K_{lidar}^{mf}(z) \\ &= \frac{k}{K_{lidar}^{mf}(z)} \cdot \frac{d[K_{lidar}^{mf}(z)]}{dz} - K_{lidar}^{mf}(z) \end{aligned}. \tag{7}$$

The above nonlinear ordinary differential equation has a basic structure, namely Bernoulli equation. Based on the Klett method [28], the inversion result of K_{lidar}^{mf} can be concluded as:

$$K_{lidar}^{mf}(z) = \frac{2 \cdot \exp\{[S(\lambda_f, \sigma_f, z) - S(\lambda_f, \sigma_f, z_m)]/k\}}{\left[\frac{K_{lidar}^{mf}(z_m)}{2}\right]^{-1} + \frac{2}{k}\int_z^{z_m} \exp\{[S(\lambda_f, \sigma_f, y) - S(\lambda_f, \sigma_f, z_m)]/k\} dy}, \tag{8}$$

After obtaining K_{lidar}^{mf}, β_f can be obtained based on Eq. (6). To provide a clearer representation of the inversion process, a flowchart is illustrated in Fig. 2.

3.2. Relationship between β_f andK_{lidar}^{mf}

Based on the above analysis, it is evident that the Klett method requires a power-law relationship between β_f and K_{lidar}^{mf}. Firstly, β_f can be expressed as follows [31]:

$$\beta_f(\lambda_f, \mathrm{Chl}) = a_{ph}(\lambda_L, \mathrm{Chl})\Phi_c \frac{\lambda_L}{\lambda_f} h_c(\lambda_f) \frac{1}{4\pi}, \tag{9}$$

where Φ_c is the quantum yield of chlorophyll fluorescence, which is affected by factors such as light, nutrients and temperature; h_c is the normalized emission wavelength function of chlorophyll fluorescence, which can be expressed using a model [32], $a_{ph}(\lambda_L$, Chl) is the chlorophyll fluorescence absorption coefficient at an excitation wavelength of 532 nm, the theoretical model can be used to calculate it as follows [33]:

$$a_{ph}(\lambda_L, \mathrm{Chl}) = 0.0113 \cdot \mathrm{Chl}^{0.871}. \tag{10}$$

According to Eq. (9,10), the relationship between β_f and Chl can be established.

The inherent optical properties (IOPs) of the water are modeled as follows:

$$a(\lambda, \mathrm{Chl}) = a_w(\lambda) + 0.06A(\lambda) \cdot \mathrm{Chl}^{0.65} + a_y(\lambda, \mathrm{Chl}), \tag{11}$$

$$b(\lambda, \mathrm{Chl}) = b_w(\lambda) + b_p(\lambda, \mathrm{Chl}), \tag{12}$$

$$c(\lambda, \mathrm{Chl}) = a(\lambda, \mathrm{Chl}) + b(\lambda, \mathrm{Chl}), \tag{13}$$

where a, b and c are absorption coefficient, scattering coefficient and beam attenuation coefficient respectively, a_w is the absorption coefficient of pure seawater [34], A is the normalized spectral absorption values of phytoplankton pigments [34], a_y is the absorption coefficient of yellow substance [35], b_w is the scattering coefficient of pure water [36]; b_p is the particulate scattering

Optics EXPRESS

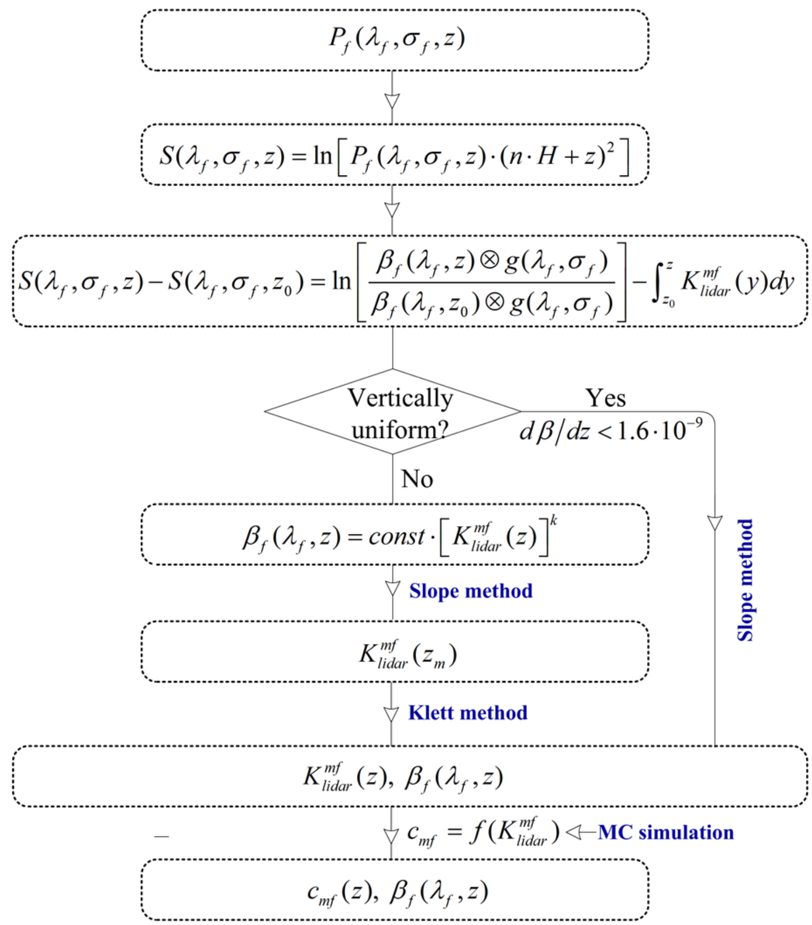

Fig. 2. Flowchart of the inversion process.

coefficient [37] and the details are shown in Table 2. c_{mf} is the sum of beam attenuation coefficient at 532 nm and 685 nm, that is:

$$c_{mf}(\mathrm{Chl}) = c(\lambda_m, \mathrm{Chl}) + c(\lambda_f, \mathrm{Chl}) \tag{14}$$

Therefore, the relationship between c_{mf} and Chl can be established based on Eq. (11–14). Then, the relationship between β_f and c_{mf} can be established through Chl. However, it is necessary to establish the relationship between c_{mf} and K_{lidar}^{mf} first before establishing the relationship between β_f and K_{lidar}^{mf}.

Subsequently, the relationship between K_{lidar}^{mf} and the IOPs of the water is established. Due to the fact that this relationship is influenced by both the hardware parameters of the lidar system and the IOPs of the water, determining this relationship requires the use of the MC simulation. MC simulation is widely recognized as a crucial tool for simulating complex processes and has been extensively employed in simulating the backscattered signal of oceanic lidars [38]. In this study, a brief introduction to MC-based simulation of backscattered signals is provided without delving into specific details. For a more comprehensive understanding of the simulation process, it is recommended to refer to a recent article [39].

Optics EXPRESS

The MC method is used to simulate the random trajectories of photon propagation in a specific medium. Both the step and direction are determined by the scattering and absorption properties of the medium. The step refers to the distance or interval traveled during each random sampling iteration, while the direction denotes the path taken by the photon. The MC method ignores the photon's wave properties, and the propagation of laser signal in the water is acted as the combination of many photon trajectories. The attenuation of laser energy is determined by three factors: the absorption of medium, the scattering probability, and the probability distribution of the steps. Thus, the MC method is widely utilized to simulate the photon propagation trajectories and monitor the energy changes. To enhance the utilization efficiency of individual photons, a semi-analytic MC model is applied [39]. This model allows for the calculation of the expected energy value and position recording of each photon within the FOV of the telescope. Note that the key parameters of the fluorescence lidar have been listed in Table 1, and the hardware parameters used during the MC simulation process match those of the fluorescence lidar.

Table 1. Key parameters of the fluorescence lidar system

	Parameter	Value
Pulsed laser	Wavelength	532 nm
	Pulse duration	501 ps
	Average power	1 W
	Pulse repetition rate	1 MHz
	Radius of laser beam	2 mm
	Divergence angle	0.5 mrad
Receiver	Focal length	50.8 mm
	Mode-field diameter of the MMF	105 µm
	Effective aperture	22.4 mm
	Bandwidth of the fluorescence filter	10 nm
	Center of the fluorescence filter	685 nm
SPCM	Detection efficiency at 685 nm	62%
	Dark count rate	50 cps

Table 2. The bio-optical models used in the MC simulation

Empirical relationships	Applicable range of Chl	References
$\begin{cases} a_y(\lambda) = a_y(440)\exp[-0.014(\lambda - 440)] \\ a_y(440) = 0.2[a_w(440) + 0.06A(440) \cdot \mathrm{Chl}^{0.65}] \end{cases}$	0.02-20 mg/m^3	[35]
$b_w(\lambda) = 0.0046(450/\lambda)^{4.32}$	-	[36]
$b_R(\lambda) = 2.6 \times 10^{-4}(488/\lambda)^{5.5}$	-	[37]
$b_p(\lambda) = 0.3\mathrm{Chl}^{0.62}(550/\lambda)$	0.03-30 mg/m^3	[37]

In the simulations, a widely used Petzold phase function was adopted [40]. With a sampling length of 10 m and a sampling interval of 0.1 m, a total of 100 sampling points can be obtained. As shown in Fig. 3(a), the simulated fluorescence backscattering signal decays exponentially. To mitigate the effects of multiple scattering in the lidar backscatter signal, a small-aperture telescope with a narrow FOV is employed.

As shown in Fig. 3(a), when the Chl is low, the percentage of multiple scattering (PMS), which includes secondary scattering and higher-order scattering, is low. Consequently, the lidar signal is predominantly governed by single scattering. However, as the Chl increases, the PMS increases. Afterwards, K_{lidar}^{mf} at different Chl is obtained by selecting the original signal with a PMS less

Optics EXPRESS

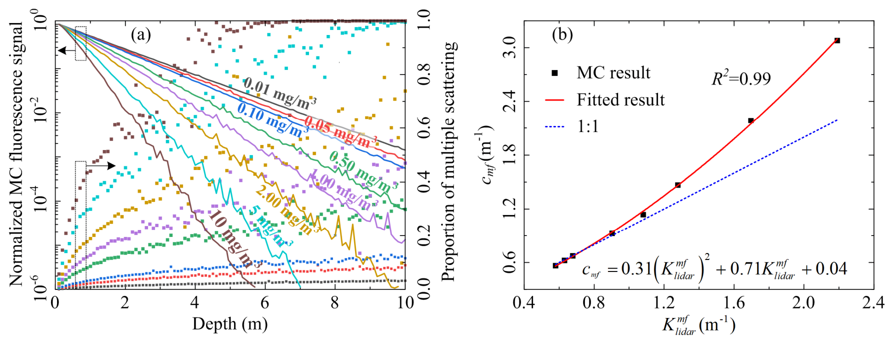

Fig. 3. (a) Simulate fluorescence backscattered signals (lines) and the percentage of multiple scattering (PMS) in the signals (scatters) for Chl ranging from 0.01 to 10 mg/m^3 using the Petzold phase function [40]. (b) Relationships between K_{lidar}^{mf} and c_{mf}, where scatter represents the results of MC simulations, and the solid line represents the fitted results.

than 100% and using the slope method [23]. The relationship between K_{lidar}^{mf} and c_{mf} is presented in Fig. 3(b). Subsequently, a second-order polynomial is used to fit the relationship between K_{lidar}^{mf} and c_{mf}. The fitting results are shown in Fig. 3(b), with a high degree of correlation indicated by the R-Square (R^2) value of 0.99. From Fig. 3(b), it can be observed that when Chl is low, K_{lidar}^{mf} is approximately equal to c_{mf}. As Chl increases, PMS increases, leading to an increasing difference between K_{lidar}^{mf} and c_{mf}. The conclusion is consistent with the finding that K_{lidar}^{mf} tends to closely align with the c_{mf} when the lidar backscattered signal is predominantly governed by quasi-single scattering, whereas the lidar attenuation coefficient is given by the K_d when the backscattered signal is primarily influenced by multi-scattering [41].

Subsequently, the relationship between c_{mf} (comprising the beam attenuation coefficient at 532 nm and 685 nm) and K_{lidar}^{mf} is established through the MC simulation. This relationship is depicted in Fig. 3(b) and can be expressed as follows:

$$c_{mf} = 0.31 \cdot (K_{lidar}^{mf})^2 + 0.71 \cdot K_{lidar}^{mf} + 0.04. \tag{15}$$

Existing models [31,34–36] were utilized to establish separate relationships between β_f and Chl, as well as between c_{mf} and Chl. By considering Chl as the pivot, the relationship between

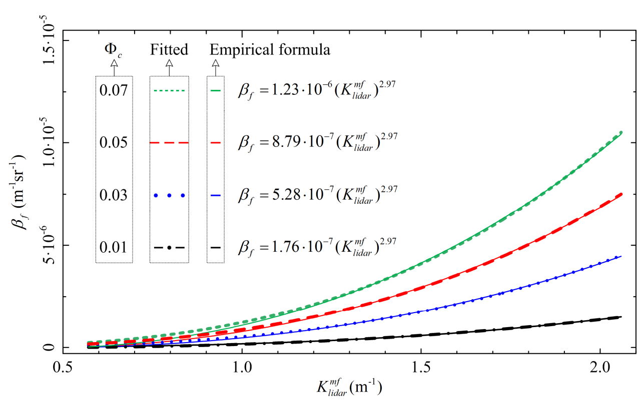

Fig. 4. Relationship between β_f and K_{lidar}^{mf} for Φ_c values of 0.01, 0.03, 0.05, and 0.07. Among them, the solid line represents the relationship given by the empirical model, and the dashed line is the fitted result.

Optics EXPRESS

β_f and c_{mf} was subsequently determined. Subsequently, based on Eq. (15), the relationship between β_f and K_{lidar}^{mf} can be established. According to the specified range (~0.005-0.07) of Φ_c [42], Fig. 4 depicts the relationship between β_f and K_{lidar}^{mf} for different values of Φ_c (0.01, 0.03, 0.05, and 0.07), with the Chl ranging from 0.01 mg/m^3 to 10 mg/m^3. Notably, the power index k remains constant regardless of Φ_c. While *const* varies with Φ_c, it has been established in Section 3 that the value of const does not affect the inversion result. Hence, the Klett inversion algorithm can be applied, utilizing the power law relationship between β_f and K_{lidar}^{mf}, where k is determined as 2.97.

4. Inversion error analysis

In this section, the errors caused by the inversion algorithm will be analyzed. It should be noted that this analysis exclusively focuses on the errors originating from the inversion algorithm, while excluding errors that arise from the SNR of the lidar backscattered signal. Four typical vertical distribution models of Chl will be used for analysis, representing the waters of North Benguela [43], North Western Shelf [44], surrounding Europe [45], and acidic lakes [46], respectively. The vertical distribution profiles of these four chlorophyll profiles are shown in Fig. 5.

To calculate the errors, firstly, it is needed to reconstruct the fluorescence backscattered signal. Based on the four vertical distribution models of Chl in Fig. 5, utilizing the bio-optical models of Eqs. (11–13), the value of c_{mf} is calculated. Then referring to the relationship between c_{mf} and K_{lidar}^{mf} of Eq. (15), the vertical profile of K_{lidar}^{mf} can be obtained. In addition, according to the vertical distribution models of Chl and the empirical relationship of β_f in Eq. (9), the vertical profile of β_f can be acquired. Finally, based on the reconstruction of K_{lidar}^{mf} and β_f, along with the assumption of B_f, P_f can be reconstructed based on Eq. (1).

After obtaining the reconstructed signal, the inversion is performed using the iterative method mentioned in Section 3, the initial value of the iterative method is calculated by using the slope method on the farthest end of the signal. According to the assumed relationship in Eq. (6), combined with Fig. 4, the inversion result of K_{lidar}^{mf} and β_f can be obtained. By utilizing the relationship between c_{mf} and K_{lidar}^{mf} shown in Eq. (15), the vertical distribution profile of c_{mf} can be obtained. Finally, based on the bio-optical models of Eq. (11–13), the Chl vertical profile can be further inverted. After obtaining the inversion values, the respective deviations from the true values, denoted as $Error_c$ (error for c_{mf}), $Error_\beta$ (error for β_f) and $Error_{\mathrm{Chl}}$ (error for Chl) can be calculated as follows:

$$Error_c = |[c_{mf}(z) - c_{mf}^{gt}(z)]/c_{mf}^{gt}(z)| \times 100\%, \tag{16}$$

$$Error_\beta = |[\beta_f(z) - \beta_f^{gt}(z)]/\beta_f^{gt}(z)| \times 100\%, \tag{17}$$

$$Error_{\mathrm{Chl}} = |[\mathrm{Chl}(z) - \mathrm{Chl}^{gt}(z)]/\mathrm{Chl}^{gt}(z)| \times 100\%, \tag{18}$$

where, c_{mf}^{gt}, β_f^{gt} and Chl^{gt} are the true value of c_{mf}, β_f and Chl respectively.

Based on the aforementioned analysis, the $Error_c$, $Error_\beta$ and $Error_{\mathrm{Chl}}$ for the four different Chl distributions are shown in Fig. 5. As shown in Fig. 5(a) and Fig. 5(b), When Chl demonstrates a linear increase or decrease with a determined slope, $Error_c$, $Error_\beta$ and $Error_{\mathrm{Chl}}$ are relatively small, which are all below 10%. In the other two scenarios depicted in Fig. 5(c) and Fig. 5(d), where Chl exhibits a layered distribution ranging from 0.01 to 10 mg/ m^3, $Error_c$, and $Error_{\mathrm{Chl}}$ are both below 15%, and although $Error_\beta$ is influenced by the assumed relationship, it remains below 20%.

Optics EXPRESS

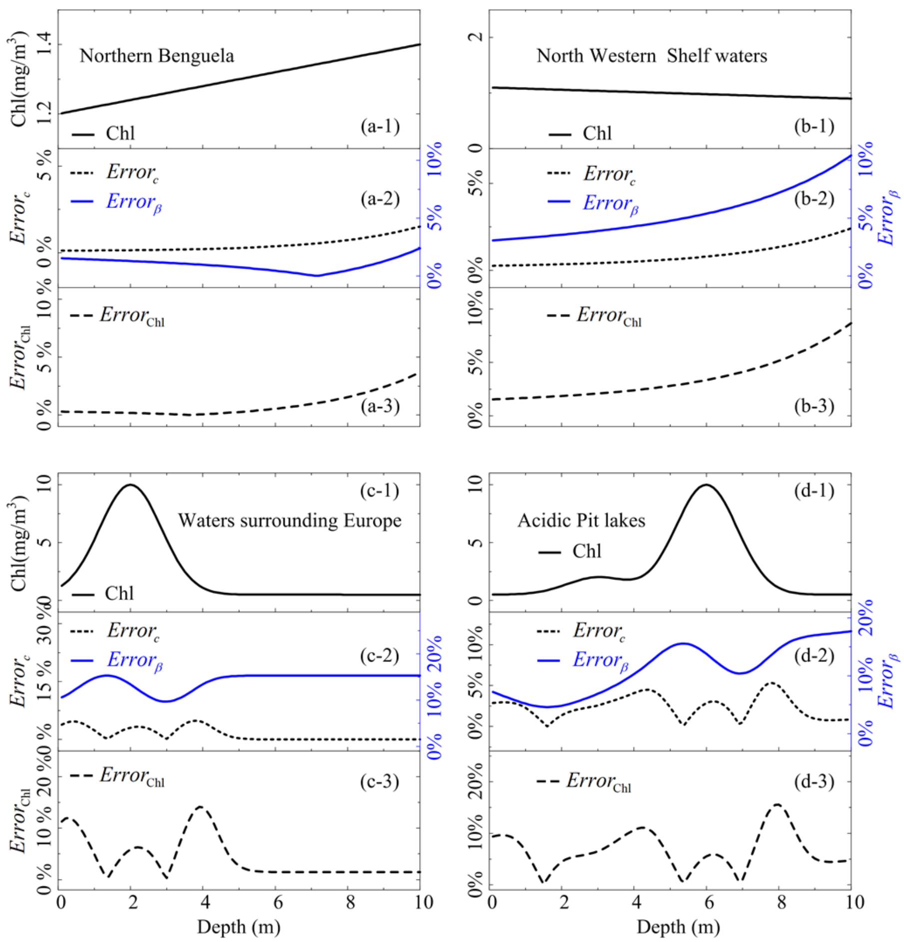

Fig. 5. Inversion errors under different vertical distributions of Chl. The sub-figures (a)-(d) show different Chl vertical distribution: (a) linearly increasing [43], (b) linearly decreasing [44], (c) unimodal with a single Gaussian distribution [45], and (d) bimodal with two Gaussian distribution [46]. Each sub-figure comprises three panels. The first panel displays the corresponding Chl vertical distribution; the second panel shows the distribution of $Error_c$ and $Error_\beta$; while the third panel displays the distribution of $Error_{\mathrm{Chl}}$.

Optics EXPRESS

5. Field experiment

To validate the effectiveness of the algorithm, the laser-induced fluorescence lidar was mounted on the R/V Experiment 3 of the Chinese Academy of Sciences. From October 10, 2023, 21:25 to October 11, 6:30, a continuous field experiment of over 9 hours was conducted at the location marked by the red pentagon in Fig. 6(a). The lidar was installed on the deck of the research vessel, positioned approximately 10 m above the water surface, and it emitted laser beams into the water at a zenith angle of 10 degrees.

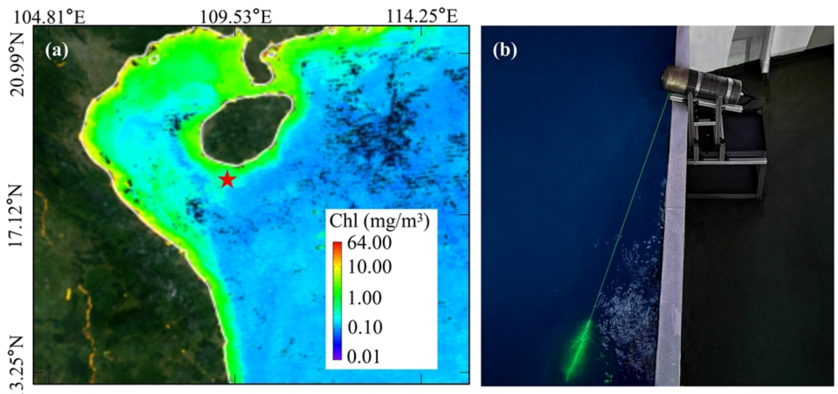

Fig. 6. (a) The location of the lidar overlaid on a monthly averaged Chl map from an ocean color satellite. (b) Photograph of the lidar in operation. Chl data sourced from NASA MODIS standard monthly composite for October 2023.

During the experiment, the fluorescence lidar accumulated photon counts every 40 s at depth intervals of 0.11 m. The spatial-temporal distribution of the logarithm of fluorescence photon count, $\ln(P_f)$, with a dynamic measurement range of approximately 30 dB, is depicted in Fig. 7(a), where the actual depth positions of photons were adjusted based on a zenith angle of 10 degrees. For the parameter inversion process, the initial value of K_{lidar}^{mf} was obtained using the slope method, followed by the inversion of β_f and K_{lidar}^{mf} using the Klett method. The c_{mf} profile was derived from the inverted K_{lidar}^{mf} and the relationship established between c_{mf} and K_{lidar}^{mf} from Eq. (15) using the MC method. The c_{mf} and β_f profiles are shown in Fig. 7(b) and 7(c), respectively. Lastly, based on the biogeochemical model presented in Table 2, Chl was obtained through the inversion of c_{mf} profile data, as shown in Fig. 7(d).

The results in Fig. 7(d) indicate that the Chl in the area mostly remains below 1 mg/m^3, which is consistent with the results shown in Fig. 6(a) obtained from water color satellite remote sensing. Furthermore, from Fig. 7(b-d), it can be observed that the Chl in the 0-2 m depth range is generally higher than that in the 2-4 m depth range. The typical vertical distribution of chlorophyll is shown in Fig. 7(e-f), with the respective observation times being October 10 at 22:00, October 11 at 00:10, and October 11 at 03:00. Additionally, a low Chl is observed between 23:00 and 02:00, as indicated by the values at a depth of 1 m in the figure. This may be related to the feeding behavior of zooplankton during that period, although further investigation is needed to determine the exact reasons. Overall, laser-induced fluorescence lidar provides a new approach for subsurface phytoplankton detection, enabling the observation of dynamic changes in aquatic phytoplankton with high temporal and depth resolution.

Optics EXPRESS

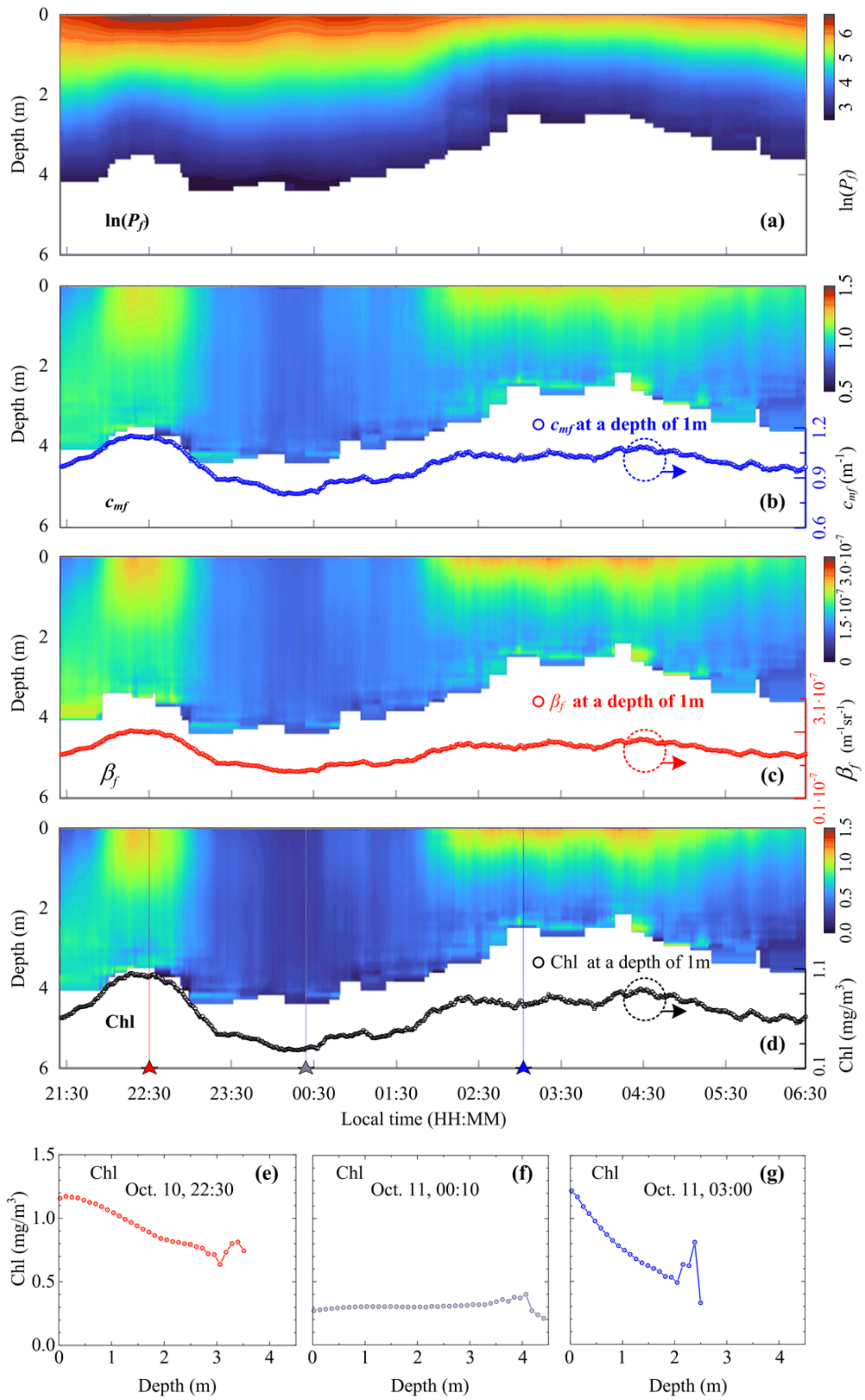

Fig. 7. Field experiment results: (a) measured fluorescence backscattered signal presented as the natural logarithm of photon count, i.e., ln(P_f), accompanied by lidar-inverted (b) c_{mf}, (c) β_f, and (d) Chl, each including their respective time series at a depth of 1 m. Typical Chl vertical distributions at (e) October 10, 22:30, (f) October 11, 00:10, (g) October 11, 03:00.

6. Conclusion

In this study, we propose and demonstrate an algorithm that can accurately retrieve the profiles of β_f and K_{lidar}^{mf} from fluorescence oceanic lidar simultaneously. To the best of our knowledge, this is the first time that β_f and K_{lidar}^{mf} profiles have been retrieved simultaneously using single-photon fluorescence lidar. This provides a pathway to improve the capability of fluorescence lidar for phytoplankton detection by inverting a_{ph} based on β_f and retrieving c_{mf} based on K_{lidar}^{mf}.

In terms of hardware, the adoption of single-photon detection technology enables fluorescence lidar to obtain profiles of phytoplankton fluorescence signals, laying the foundation for simultaneous retrieval of β_f and K_{lidar}^{mf}. In terms of algorithms, theoretical analysis verifies that the relationship between β_f and K_{lidar}^{mf} in our single-photon fluorescence lidar can be expressed by a power-law exponent, satisfying the conditions for using the Klett algorithm. In the process of establishing the relationship between β_f and K_{lidar}^{mf}, the shipborne single-photon fluorescence lidar adopts a small beam laser and a small-aperture telescope, which tends to make K_{lidar}^{mf} serve as the c_{mf} of IOPs, facilitating the establishment of the relationship between β_f and K_{lidar}^{mf}. The feasibility and effectiveness of the algorithm in fluorescence oceanic lidar are demonstrated through theoretical analysis and field experiments.

In future work, we will further validate the applicability of the relationship between β_f and K_{lidar}^{mf} under case 2 water conditions, as it was initially established based on case 1 water conditions. Additionally, a comprehensive comparison between fluorescence lidar measurements and in-situ data, as well as ocean color remote sensing results, will be conducted to optimize the algorithm. Regarding the hardware aspect of the lidar system, the broad fluorescence spectrum and the wide bandwidth of the fluorescence filter (10 nm) pose a challenge when employing single-photon detection, as they make the system susceptible to interference from solar radiation noise. To address this issue, the plan will be to integrate the miniaturized fluorescence lidar into underwater platforms, as demonstrated in our previous research [24,47,48]. This deployment will help eliminate interference arising from the air-sea interface and mitigate the impact of solar radiation noise on our detection capabilities. We believe that this work will be an important complement to color remote sensing of phytoplankton, deepening our understanding of the spatiotemporal distribution and dynamic changes of marine phytoplankton.

Funding. National Key Research and Development Program of China (2022YFB3901704); Blue Carbon Ecosystem Assessment, Restoration and Accounting: A Tencent supported project; Innovation Program for Quantum Science and Technology (No. 2021ZD0303102); Joint Funds of the National Natural Science Foundation of China (No. U2106210); Natural Science Foundation of Fujian Province (No. 2020J01026); Fujian Provincial Central Guided Local Science and Technology Development Special Project (2022L3078); MEL-RLAB Joint Fund for Marine Science & Technology Innovation.

Acknowledgments. The authors would like to thank Zhifeng Yang, Zhenwu Weng, and Zaifa Lin for their assistance in fluorescence lidar data acquisition.

Disclosures. The authors declare no conflicts of interest.

Data availability. The data that support the findings of this study are available from the corresponding author upon reasonable request.

References

1. A. Bricaud, A. Ciotti, and B. Gentili, "Spatial-temporal variations in phytoplankton size and colored detrital matter absorption at global and regional scales, as derived from twelve years of SeaWiFS data (1998–2009)," Global Biogeochem. Cycles **26**(1), 1 (2012).
2. Z. Lee, V. P. Lance, S. Shang, *et al.*, "An assessment of optical properties and primary production derived from remote sensing in the Southern Ocean (SO GasEx)," J. Geophys. Res.: Oceans **116**, 1 (2011).
3. L. Qi, C. Hu, Q. Xing, *et al.*, "Long-term trend of Ulva prolifera blooms in the western Yellow Sea," Harmful Algae **58**, 35–44 (2016).
4. C. Jamet, A. Ibrahim, Z. Ahmad, *et al.*, "Going beyond standard ocean color observations: lidar and polarimetry," Front. Mar. Sci. **6**, 251 (2019).

Optics EXPRESS

5. J. H. Churnside and J. A. Shaw, "Lidar remote sensing of the aquatic environment," Appl. Opt. **59**(10), C92–C99 (2020).
6. L. Lacour, R. Larouche, and M. Babin, "In situ evaluation of spaceborne CALIOP lidar measurements of the upper-ocean particle backscattering coefficient," Opt. Express **28**(18), 26989–26999 (2020).
7. X. Lu, Y. Hu, Y. Yang, *et al.*, "New Ocean Subsurface Optical Properties From Space Lidars: CALIOP/CALIPSO and ATLAS/ICESat-2," Earth and Space Science **8**(10), e2021EA001839 (2021).
8. M. R. Roddewig, J. H. Churnside, and J. A. Shaw, "Lidar measurements of the diffuse attenuation coefficient in Yellowstone Lake," Appl. Opt. **59**(10), 3097–3101 (2020).
9. M. J. Behrenfeld, Y. Hu, C. A. Hostetler, *et al.*, "Space-based lidar measurements of global ocean carbon stocks," Geophys. Res. Lett. **40**(16), 4355–4360 (2013).
10. X. Lu and Y. Hu, *Estimation of particulate organic carbon in the ocean from space-based polarization lidar measurements, SPIE Asia-Pacific Remote Sensing* (SPIE, 2014), Vol. 9261.
11. J. A. Schulien, M. J. Behrenfeld, J. W. Hair, *et al.*, "Vertically-resolved phytoplankton carbon and net primary production from a high spectral resolution lidar," Opt. Express **25**(12), 13577–13587 (2017).
12. P. Chen, C. Jamet, and D. Liu, "LiDAR Remote Sensing for Vertical Distribution of Seawater Optical Properties and Chlorophyll-a From the East China Sea to the South China Sea," IEEE Trans. Geosci. Remote Sensing **60**, 1–21 (2022).
13. P. Weibring, T. Johansson, H. Edner, *et al.*, "Fluorescence lidar imaging of historical monuments," Appl. Opt. **40**(33), 6111–6120 (2001).
14. Z. Guan, M. Brydegaard, P. Lundin, *et al.*, "Insect monitoring with fluorescence lidar techniques: field experiments," Appl. Opt. **49**(27), 5133–5142 (2010).
15. H. Edner, J. Johansson, S. Svanberg, *et al.*, "Fluorescence lidar multicolor imaging of vegetation," Appl. Opt. **33**(13), 2471–2479 (1994).
16. J. Lu, Y. Yuan, Z. Duan, *et al.*, "Short-range remote sensing of water quality by a handheld fluorosensor system," Appl. Opt. **59**(10), C1–C7 (2020).
17. G. Zhao, M. Ljungholm, E. Malmqvist, *et al.*, "Inelastic hyperspectral lidar for profiling aquatic ecosystems," Laser Photonics Rev. **10**(5), 807–813 (2016).
18. H. H. Kim, "New algae mapping technique by the use of an airborne laser fluorosensor," Appl. Opt. **12**(7), 1454–1459 (1973).
19. S. R. Rogers, T. Webster, W. Livingstone, *et al.*, "Airborne Laser-Induced Fluorescence (LIF) Light Detection and Ranging (LiDAR) for the quantification of dissolved organic matter concentration in natural waters," Estuaries and coasts **35**(4), 959–975 (2012).
20. S. C. Palmer, V. V. Pelevin, I. Goncharenko, *et al.*, "Ultraviolet fluorescence LiDAR (UFL) as a measurement tool for water quality parameters in turbid lake conditions," Remote Sens. **5**(9), 4405–4422 (2013).
21. Y. Saito, K. Kakuda, M. Yokoyama, *et al.*, "Design and daytime performance of laser-induced fluorescence spectrum lidar for simultaneous detection of multiple components, dissolved organic matter, phycocyanin, and chlorophyll in river water," Appl. Opt. **55**(24), 6727–6734 (2016).
22. M. Shangguan, H. Xia, C. Wang, *et al.*, "Dual-frequency Doppler lidar for wind detection with a superconducting nanowire single-photon detector," Opt. Lett. **42**(18), 3541–3544 (2017).
23. M. Shangguan, Z. Liao, Y. Guo, *et al.*, "Sensing the profile of particulate beam attenuation coefficient through a single-photon oceanic Raman lidar," Opt. Express **31**(16), 25398–25414 (2023).
24. M. Shangguan, Z. Yang, M. Shangguan, *et al.*, "Remote sensing oil in water with an all-fiber underwater single-photon Raman lidar," Appl. Opt. **62**(19), 5301–5305 (2023).
25. Z. Lin, M. Shangguan, F. Cao, *et al.*, "Underwater Single-Photon Lidar Equipped with High-Sampling-Rate Multi-Channel Data Acquisition System," Remote Sens. **15**(21), 5216 (2023).
26. M. Shangguan, Y. Guo, Z. Liao, *et al.*, "Sensing profiles of the volume scattering function at 180° using a single-photon oceanic fluorescence lidar," Opt. Express **31**(24), 40393–40410 (2023).
27. J. H. Churnside and R. D. Marchbanks, "Inversion of oceanographic profiling lidars by a perturbation to a linear regression," Appl. Opt. **56**(18), 5228–5233 (2017).
28. J. D. Klett, "Stable analytical inversion solution for processing lidar returns," Appl. Opt. **20**(2), 211–220 (1981).
29. P. Chen, C. Jamet, Z. Zhang, *et al.*, "Vertical distribution of subsurface phytoplankton layer in South China Sea using airborne lidar," Remote Sensing of Environment **263**, 112567 (2021).
30. J. H. Churnside, J. W. Hair, C. A. Hostetler, *et al.*, "Ocean backscatter profiling using high-spectral-resolution lidar and a perturbation retrieval," Remote Sens. **10**(12), 2003 (2018).
31. L. Zotta, S. Matteoli, M. Diani, *et al.*, "AFRODiTE: A fluorescence LiDAR simulator for underwater object detection applications," IEEE Trans. Geosci. Remote Sensing **53**(6), 3022–3041 (2015).
32. C. D. Mobley, *Light and water: radiative transfer in natural waters* (Academic press, 1994).
33. A. Bricaud, M. Babin, A. Morel, *et al.*, "Variability in the chlorophyll-specific absorption coefficients of natural phytoplankton: Analysis and parameterization," J. Geophys. Res.: Oceans **100**(C7), 13321–13332 (1995).
34. L. Prieur and S. Sathyendranath, "An optical classification of coastal and oceanic waters based on the specific spectral absorption curves of phytoplankton pigments, dissolved organic matter, and other particulate materials 1," Limnol. Oceanogr. **26**(4), 671–689 (1981).
35. Z. Lee and J. Tang, "The two faces of "Case-1" water," Journal of Remote Sensing (2022).

Optics EXPRESS

36. A. Morel, "Optical properties of pure water and pure seawater," Optical aspects of oceanography **1**, 1 (1974).
37. A. Morel, "Optical modeling of the upper ocean in relation to its biogenous matter content (case I waters)," J. Geophys. Res.: Oceans **93**(C9), 10749–10768 (1988).
38. D. J. Spence, B. R. Neimann, and H. M. Pask, "Monte Carlo modelling for elastic and Raman signals in oceanic LiDAR," Opt. Express **31**(8), 12339–12348 (2023).
39. S. Chen, P. Chen, L. Ding, *et al.*, "A New Semi-Analytical MC Model for Oceanic LIDAR Inelastic Signals," Remote Sens. **15**(3), 684 (2023).
40. T. J. Petzold, "*Volume scattering functions for selected ocean waters*," (Scripps Institution of Oceanography La Jolla Ca Visibility Lab, 1972).
41. H. R. Gordon, "Interpretation of airborne oceanic lidar: effects of multiple scattering," Appl. Opt. **21**(16), 2996–3001 (1982).
42. S. Maritorena, A. Morel, and B. Gentili, "Determination of the fluorescence quantum yield by oceanic phytoplankton in their natural habitat," Appl. Opt. **39**(36), 6725–6737 (2000).
43. E. Gutknecht, I. Dadou, B. Le Vu, *et al.*, "Coupled physical/biogeochemical modeling including O 2-dependent processes in the Eastern Boundary Upwelling Systems: application in the Benguela," **10**, 3559–3591 (2013).
44. S. Miladinova, A. Stips, D. Macias Moy, *et al.*, "Seasonal and Inter-Annual Variability of the Phytoplankton Dynamics in the Black Sea Inner Basin," in *Oceans*, (MDPI, 2020), 251–273.
45. H. Loisel, D. Stramski, B. G. Mitchell, *et al.*, "Comparison of the ocean inherent optical properties obtained from measurements and inverse modeling," Appl. Opt. **40**(15), 2384–2397 (2001).
46. J. Sánchez-España, C. Falagán, D. Ayala, *et al.*, "Adaptation of Coccomyxa sp. to extremely low light conditions causes deep chlorophyll and oxygen maxima in acidic pit lakes," Microorganisms **8**(8), 1218 (2020).
47. M. Shangguan, Z. Yang, Z. Lin, *et al.*, "Compact long-range single-photon underwater lidar with high spatial-temporal resolution," IEEE Geosci. Remote Sensing Lett. **20**, 1–5 (2023).
48. M. Shangguan, Z. Weng, Z. Lin, *et al.*, "Day and night continuous high-resolution shallow-water depth detection with single-photon underwater lidar," Opt. Express **31**(26), 43950–43962 (2023).